Role of sacrificial Fe sites in making a 2D heterostructure as an efficient catalyst for oxygen evolution reaction in seawater

Suraj Loomba[a], Muhammad Waqas Khan[b], Ashakiran Maibam[c], Muhammad Haris[a], Sharafadeen Gbadamasi[a], Vasundhara Nettem[b], Seyedmahdi Mousavi[a], Anton Tadich[d], Lars Thomsen[d], Karishma Jain[b,e], Babar Shabbir[b], Asif Mahmood[f], Ravichandar Babarao[g,h,i]*, Jian Xian[j], and Nasir Mahmood[b]*

[a]*School of Engineering, RMIT University, Victoria, 3000, Australia*
[b]*School of Science, RMIT University, Victoria 3001, Australia*
Email: nasir.mahmood@rmit.edu.au
[c]*ICGM, University of Montpellier, CNRS, ENSCM, Montpellier, France*
[d]*Australian Synchrotron, ANSTO, 800 Blackburn Road, Clayton, Victoria, 3168, Australia*
[e]*Advanced Carbon Products and Metrology Department, CSIR- National Physical Laboratory (CSIR-NPL), New Delhi 110012, India*
[f]*School of Mathematical and Physical Science, University of Technology Sydney, Sydney, New South Wales, 2007, Australia*
[g]*School of Science, Centre for Advanced Materials and Industrial Chemistry (CAMIC), RMIT University, Melbourne 3001, Victoria, Australia*
[h]*CSIRO, Normanby Road, Clayton 3168, Victoria, Australia*
[i]*ARC Centre of Excellence for Green Electrochemical Transformation of Carbon Dioxide, School of Science, RMIT University, Melbourne 3000, Australia*
[j]*School of Materials and Energy, University of Electronic Science and Technology of China, Chengdu, 611731, China*

Experimental Methods

Material Characterization

To analyze the morphology, crystal structure, and lattice imperfections, transmission electron microscope (TEM), high-resolution TEM analysis, and energy-dispersive X-ray spectroscopy (EDS) were done by using JEOL 2100F instrument. X-ray diffraction (XRD) analysis was done using a Bruker D4 Endeavor to obtain the crystal structure of the products. High-resolution X-ray photoelectron spectroscopy (XPS) was conducted by using a thermo-scientific K-alpha system. The system consists of an Al Kα monochromated X-ray source for scanning the samples at a dwell time of 50 ms^{-1} and pass time of 50 eV. Raman spectra were obtained using

a LabRAM HR evolution Raman spectrometer (Horiba Scientific) under a 532 nm laser with 50 mW power. Perklin Elmer Spectrum 100 Fourier-transform infrared (FIR-FTIR) spectroscopy was used to study the spectra ranging between 200 and 00 cm^{-1}. A CHI 760D electrochemical workstation (CH Instruments) was used for the electrochemical measurements. Near edge X-ray absorption fine structure (NEXAFS) data was acquired using the High Throughput NEXAFS endstation at the soft X-ray beamline, Australian Synchrotron in Partial Electron Yield (PEY) mode using a retarding grid-based channeltron detector set to an appropriate bias for each element. The gas chromatography was done using Varian gas chromatograph with single quadrupole mass spectrometer (GC-MS). The gas chromatography was performed using a Varian gas chromatograph with a single quadrupole mass spectrometer (GC-MS). The Agilent inductively coupled plasma mass spectrometer (ICP-MS) with laser ablation 2 capability was used to acquire the ICP-MS results.

Electrochemical measurements

The electrochemical testing of the as-prepared samples was done in 1.0 M KOH, and seawater electrolytes at ambient temperature and pressure using a CHI 760 D electrochemical workstation (CH Instruments) in which saturated Hg/HgO was used as the reference electrode, a graphite rod as the counter electrode, and the working electrode was prepared by drop-casting the samples on nickel foam which was washed with dilute HCl and water before electrode preparation. The polarization curves were recorded with a scan rate of 5 mV s^{-1} after iR correction. The powdered sample was added to the carbon black solution (4:1), followed by the addition of Polytetrafluoroethylene (PTFE) solution (60% in H$_2$O, sigma) and sonicated to form a homogeneous ink. The carbon black solution was prepared by adding 20 mg carbon to a 20 mL mixture of Isopropyl alcohol (IPA) and water (1:4). The solution was then sonicated for 1h to acquire proper dispersion. Then, 200 μL of the ink was drop-casted onto an area of 0.25 cm^2 on nickel foam. For determining the electrochemical double-layer capacitance (C$_{dl}$), electrochemical cyclic voltammetry (CV) measurements were performed over a range of scan rates (10, 20, 30, 40, and 50 mV s^{-1}). Electrochemical impedance spectroscopy (EIS) was carried out over the frequency range of 1 to 10,000 Hz using an AC voltage of 5 mV amplitude. The stability tests were also performed at a fixed potential.

Diethyl-p-phenylene diamine (DPD) test

The DPD test measures chlorine in various forms, such as free, combined, or total chlorine residuals. 10 mL of natural seawater and electrolyte (post-testing) was taken in a glass vial, and

the pH of the solvents was adjusted between 7-8 by using acetic acid followed by the addition of 2 μL DPD.

Density functional theory calculations

Computational calculations on model FeO(111), MoO$_2$(-111), and MO@FO surfaces were performed using density functional theory (DFT) as implemented in the Vienna *ab initio* simulation package (VASP).[11.12] A generalized gradient approximation (GGA) method was employed with the Perdew-Burke-Ernzerhof (PBE) exchange correlation to define the ion-electron interaction of the electrons defined using the projector augmented wave (PAW) method.[13] An energy cutoff of 400 eV was applied, with a *k*-point mesh of 2 x 2 x 1 for the geometry optimization with the van der Waals forces were accounted by the Grimme DFT-D3 method with Becke-Johnson damping function.[14] For the geometry optimization calculations, the atomic positions were relaxed until the total energy was converged to 1 x 10^{-5} eV and the Hellman-Feynman force on each relaxed atom was less than -0.05 eV/Å. A vacuum spacer of 20 Å was inserted along the *z*-direction to avoid interlayer interactions. The adsorption energy (E_{ad}) of the reactant gas species or OER intermediates on the oxide surfaces was calculated as follows:

$$E_{ad} = (E_{total} - (E_{oxides} + E_{gas-species})) \tag{1}$$

where E_{total} is the total energy of the intermediate geometry; E_{oxides} is the total energy of the oxide surface and $E_{gas-species}$ is the electronic energy of the gas species or OER intermediates. The OER mechanism on FeO, MoO$_2$ surfaces, and MO@FO heterostructure have been investigated to evaluate the oxygen evolution efficiency and investigate the active center of OER on the surfaces. The change in Gibbs free energy, ΔG of the reaction mechanism along the reaction coordinates has been computed to explore the reaction mechanism, and ΔG has been calculated as,

$$\Delta G = \Delta E - \Delta ZPE - T\Delta S \tag{2}$$

where ΔE is the change in electronic energy, ΔZPE is the change in zero-point energy, and ΔS is the entropy correction at room temperature (298.15 K) obtained from non-imaginary frequencies of the OER intermediates. The potential rate-determining step (PDS) for the OER reaction is the single step with the highest free energy change (ΔG$_{max}$), and the limiting potential, U$_{OER}$ is equal to –(ΔG$_{max}$)/e. The corresponding theoretical OER overpotential, η$_{OER}$ = U$_{SHE}$ – U$_{OER,}$ where U$_{SHE}$ = 1.23 V for the standard H$_2$O/O$_2$ reduction reaction.

Supporting Results and Data
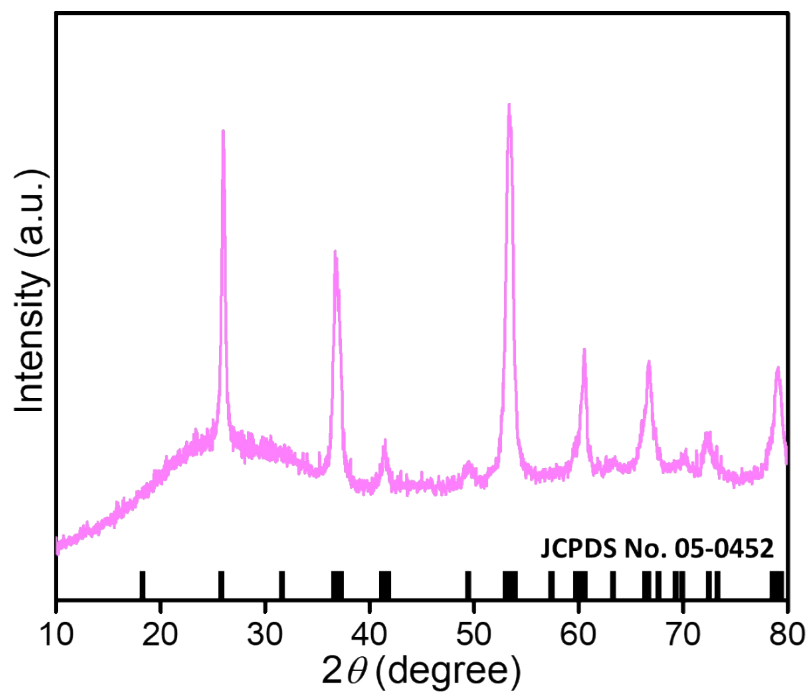
Figure S1. XRD of MoO$_2$ matching with JCPDS No. 05-0452.
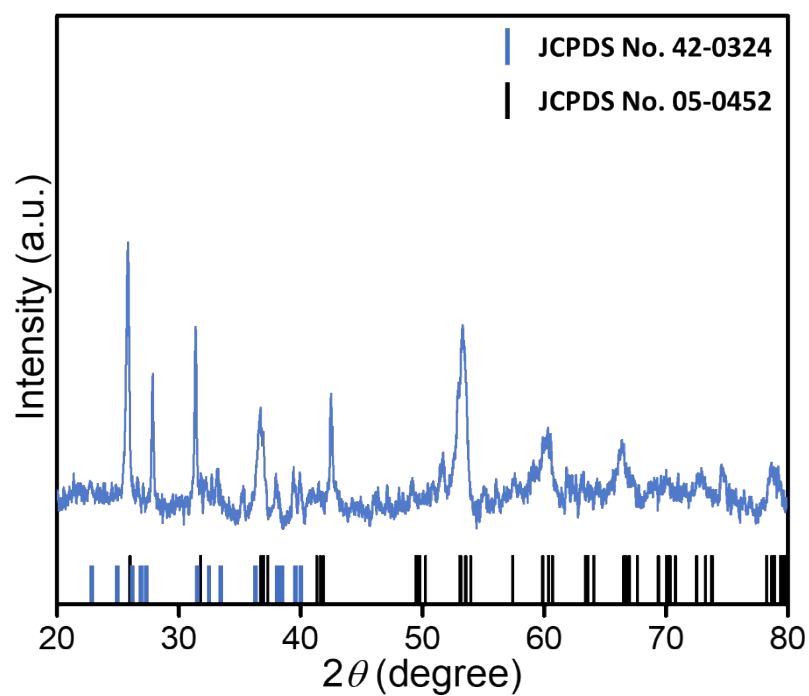
Figure S2. XRD of 320mg Fe foam in MoO$_2$ showing the presence of FeMoO$_4$ and MoO$_2$.
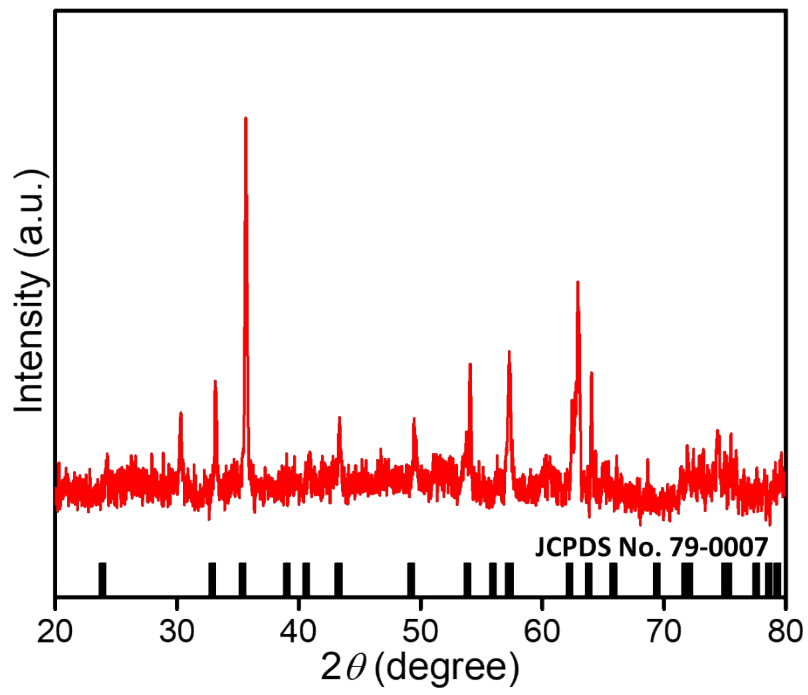
Figure S3. XRD of Fe_2O_3 matching with JCPDS No. 79-0007.
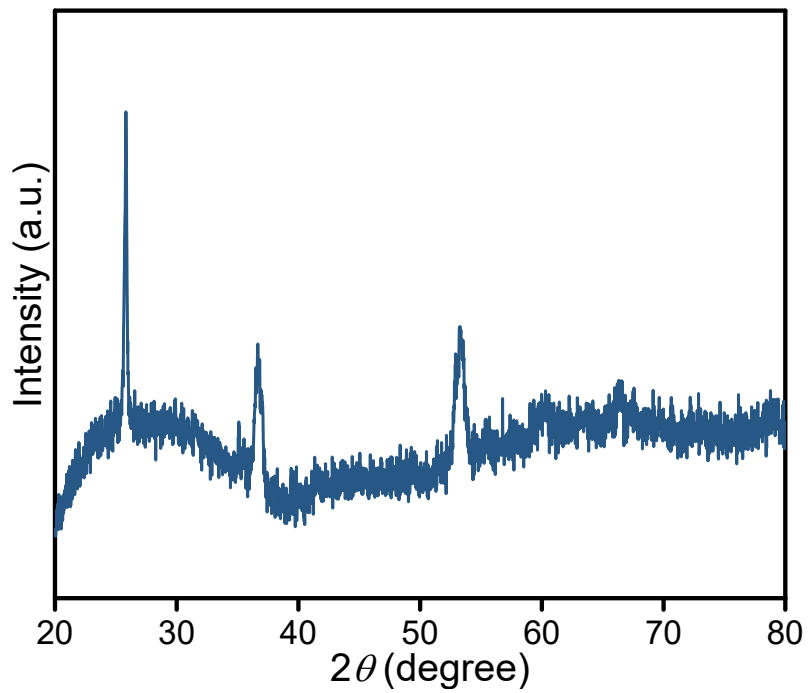
Figure S4. XRD of MO@FO before annealing showing a few peaks.
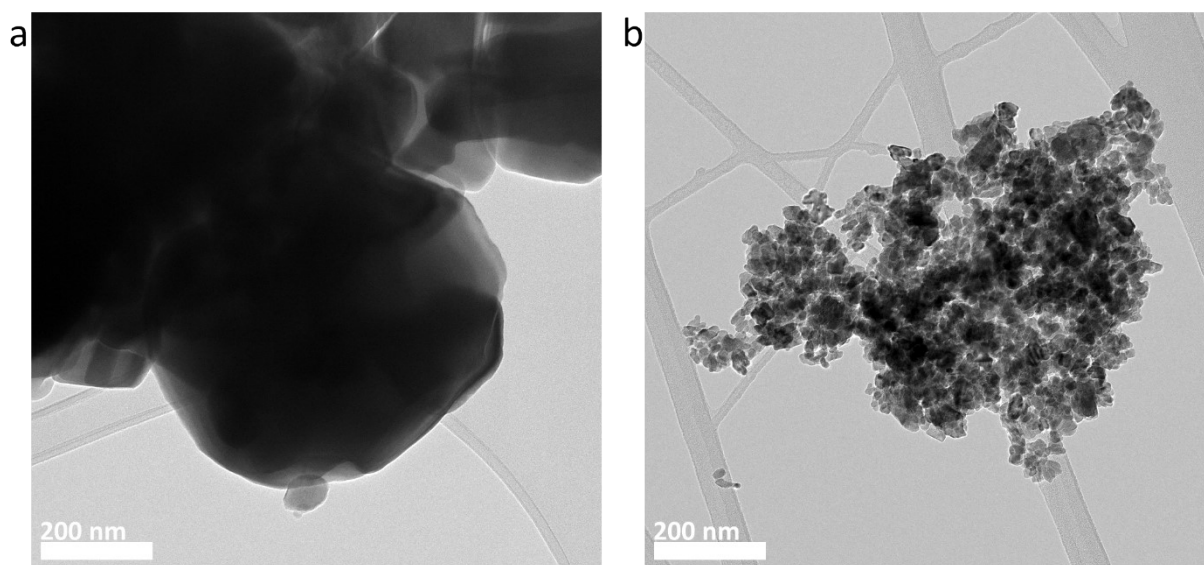
Figure S5. TEM image of (a) Fe_2O_3 showing sheet-like and (b) MoO_2 showing flake-like structure.
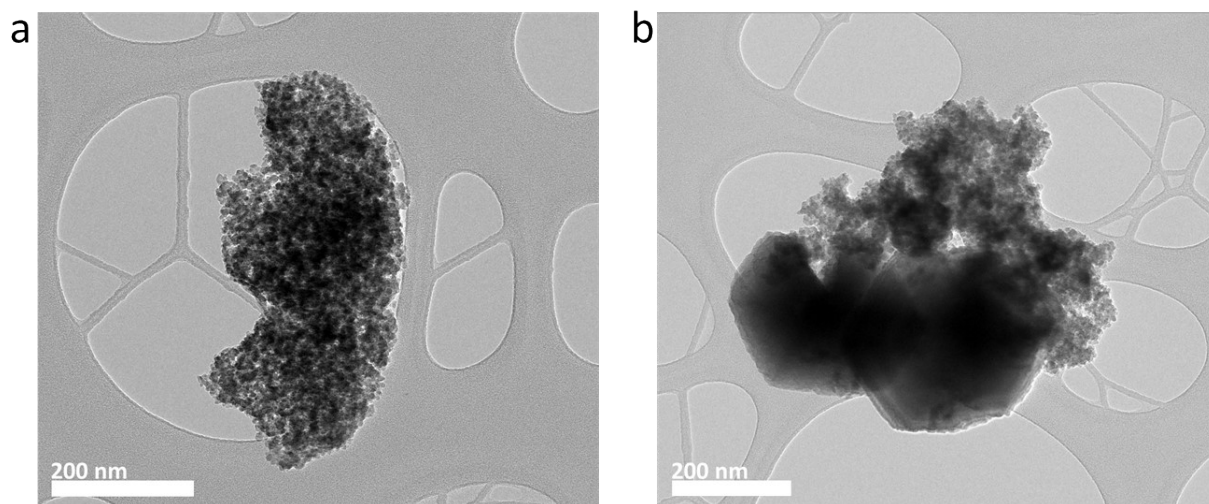
Figure S6. TEM images of the sample when Fe powder was used instead of Fe foam.
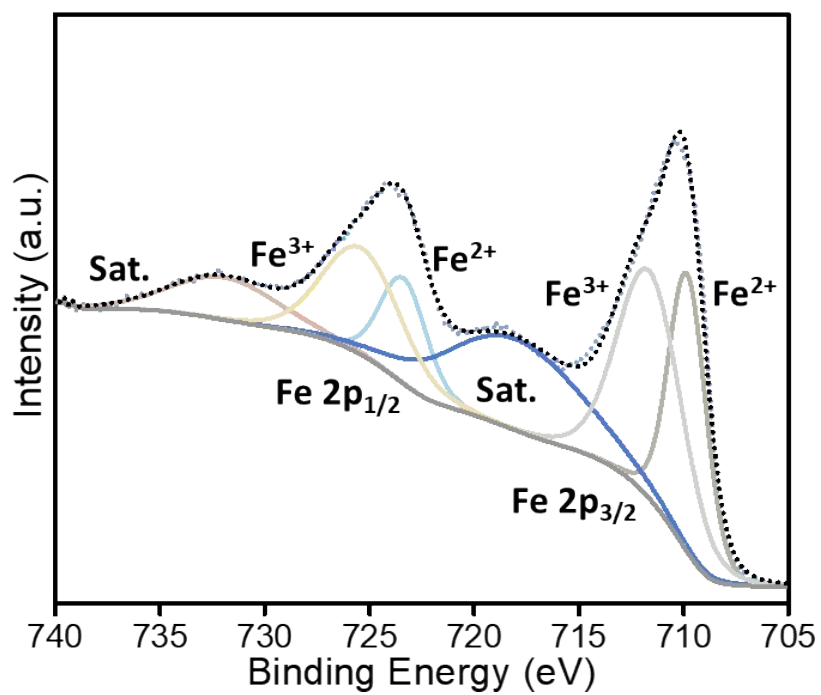
Figure S7. Fe 2p XPS spectrum of Fe_2O_3 showing the presence of Fe^{2+} and Fe^{3+} oxidation states.
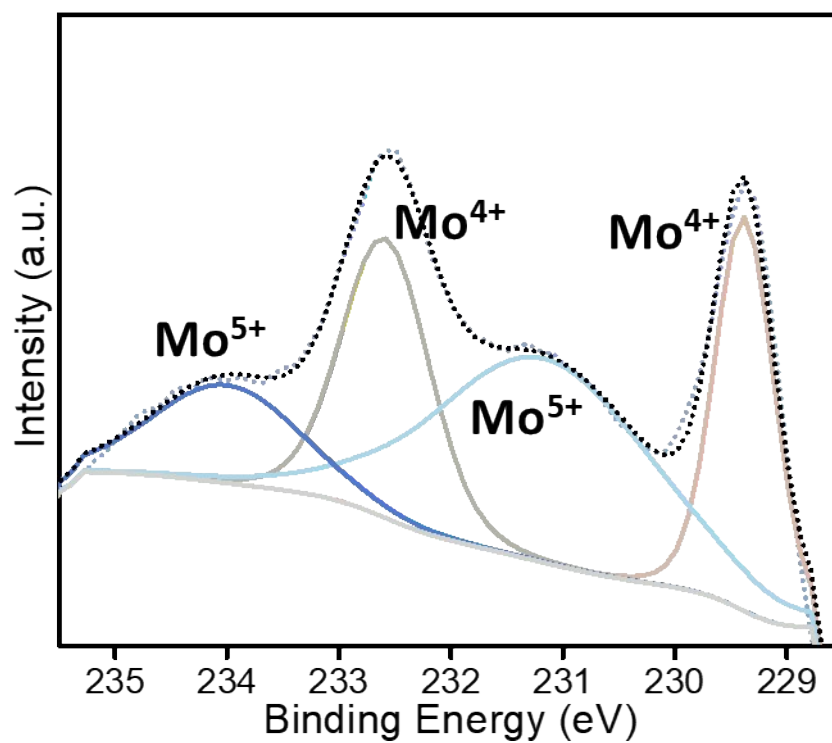
Figure S8. Mo 3d XPS spectrum of MoO_2 showing the presence of Mo^{4+}, Mo^{5+}, and Mo^{6+} oxidation states.
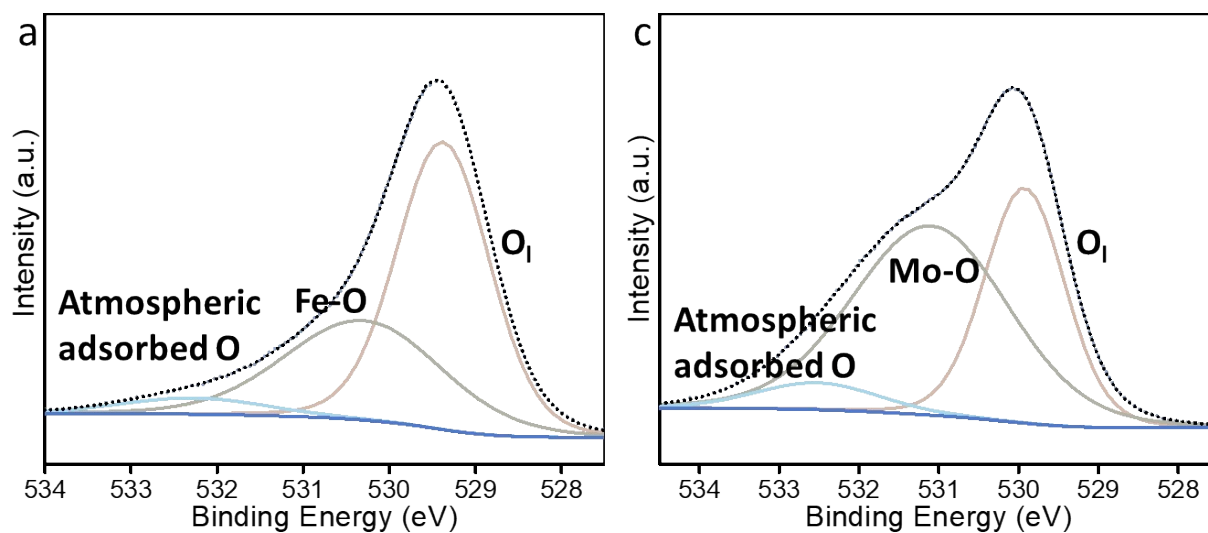
Figure S9. O 1s XPS spectrum of (a) Fe_2O_3 and (b) MoO_2 showing the presence of M-O bond.
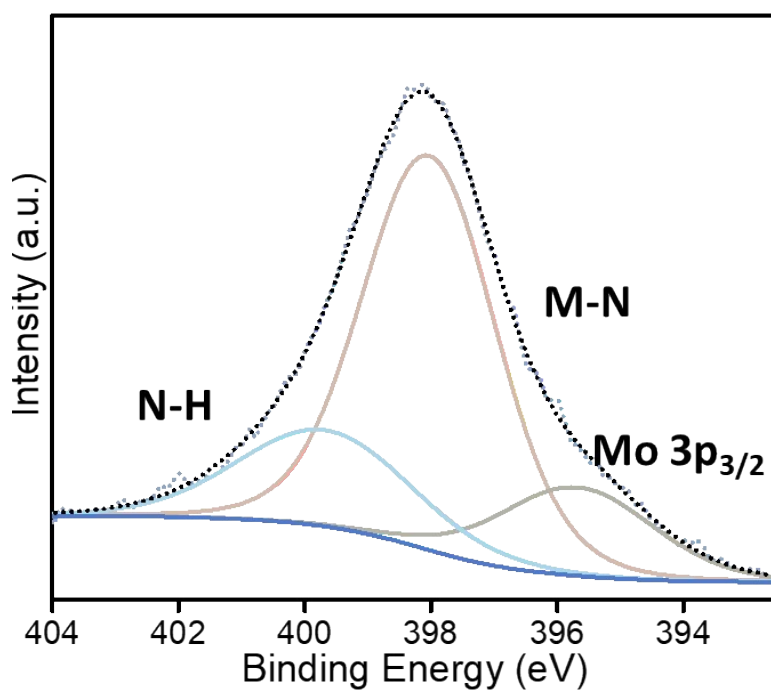
Figure S10. Deconvoluted N 1s spectra for MO@FO.
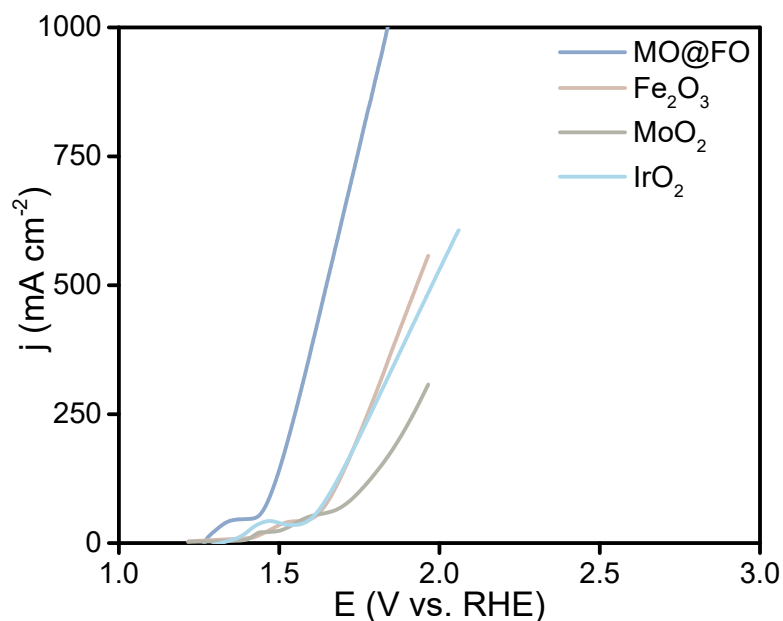
Figure S11. OER LSV curves for different samples in 1 M KOH.
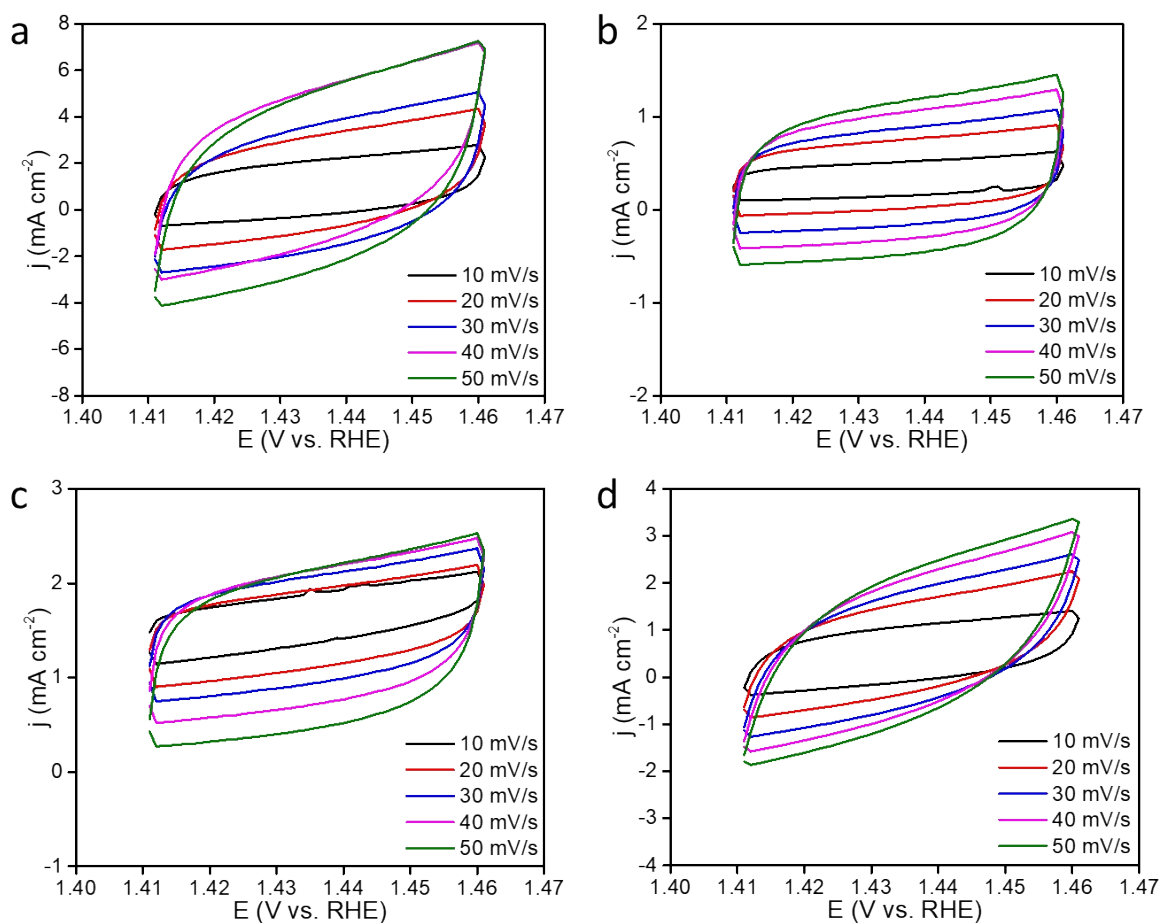
Figure S12. Cyclic voltammetry (CV) curves in the voltage range of 1.411 – 1.461 V vs. RHE, with scan rates ranging from 10 to 50 mV s-1 (a) MO@FO, (b) Fe₂O₃, (c) MoO₂, and (d) IrO₂ indicating that the heterostructure has the highest electrochemical active surface area.
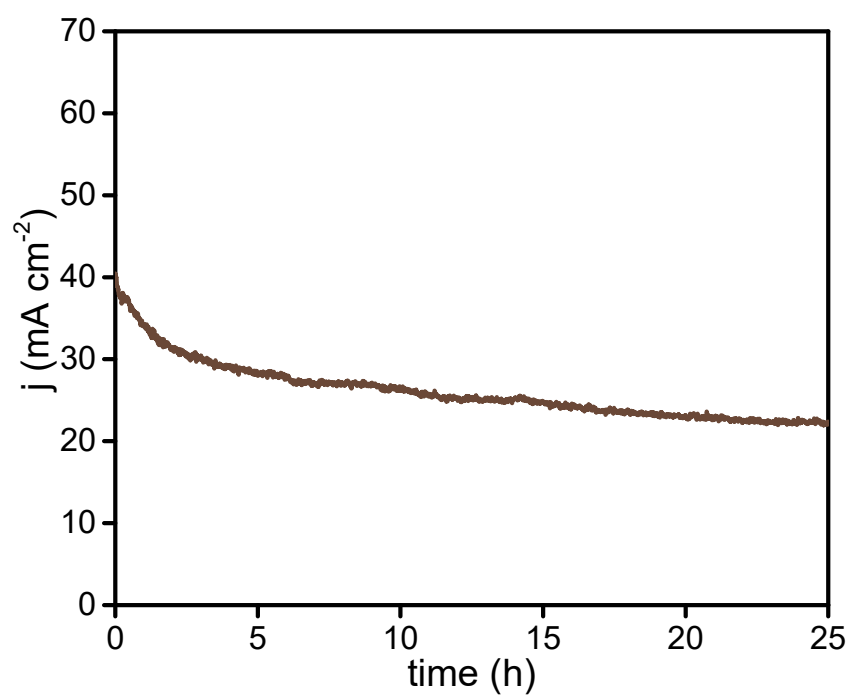
Figure S13. Long-term stability for IrO$_2$ in alkaline seawater.
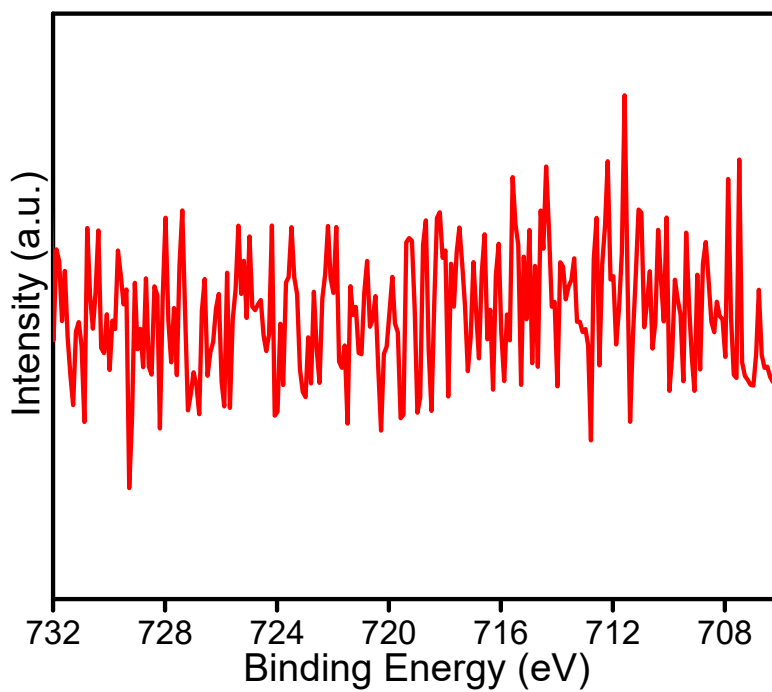
Figure S14. Post-stability (250 h) Fe 2p XPS spectrum for MO@FO in seawater showing leaching of Fe.
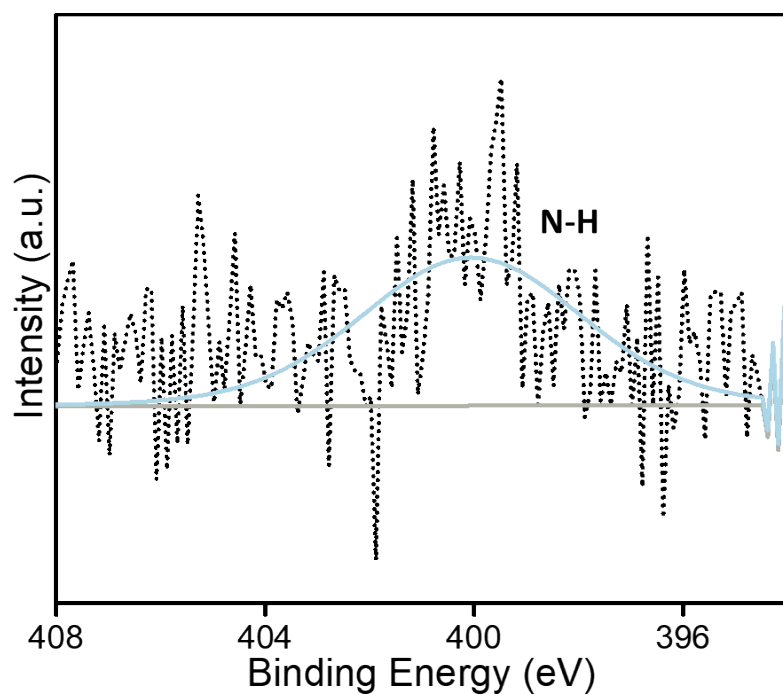
Figure S15. N 1s XPS spectrum for MO@FO after testing in 1M SW without Iron nitrate salt.
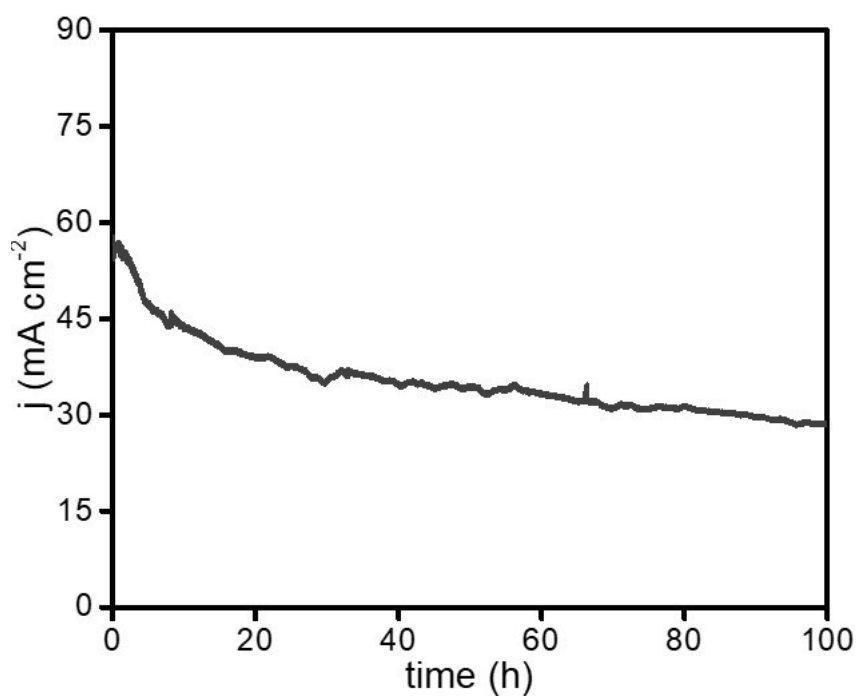
Figure S16. Stability testing for MO@FO in alkaline seawater with 0.0375 mM Iron nitrate salt.
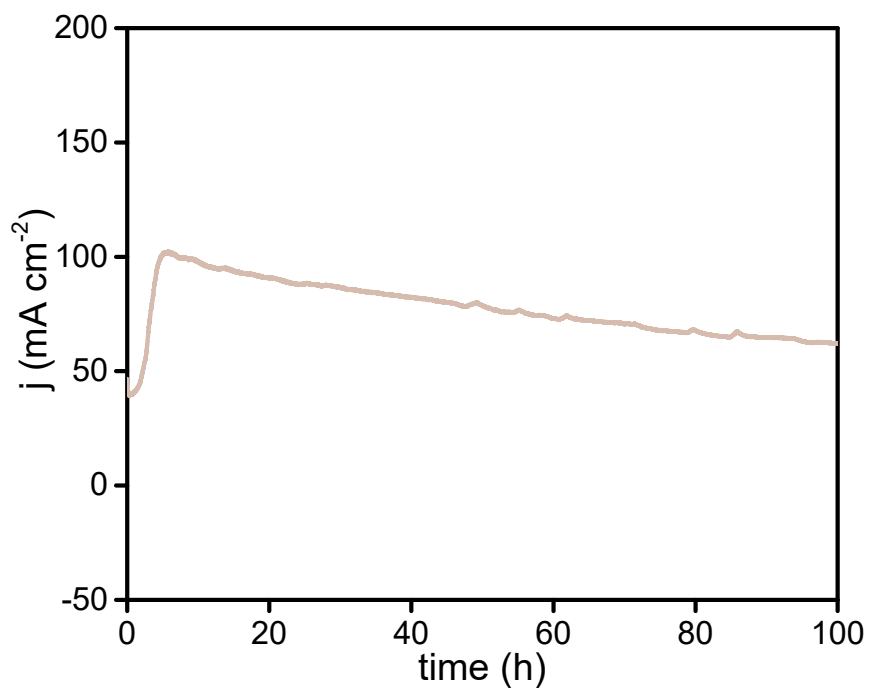
Figure S17. Stability testing for MO@FO in alkaline seawater with 0.0625 mM Iron nitrate salt.
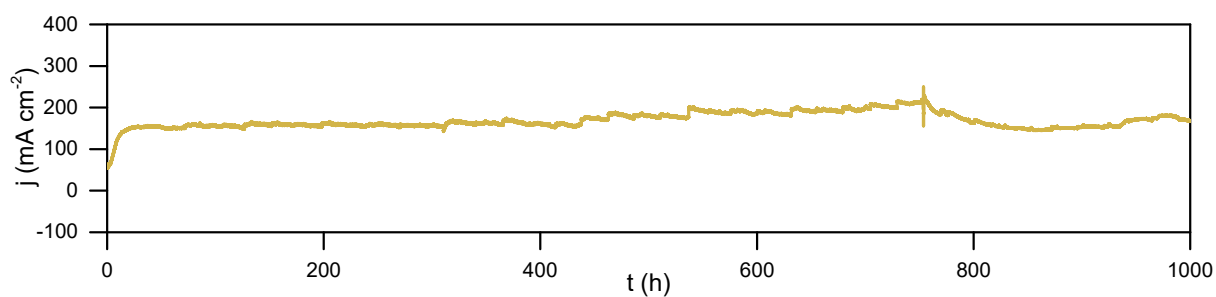
Figure S18. MO@FO 1000 h stability testing after adding iron sulphate salt in alkaline seawater.
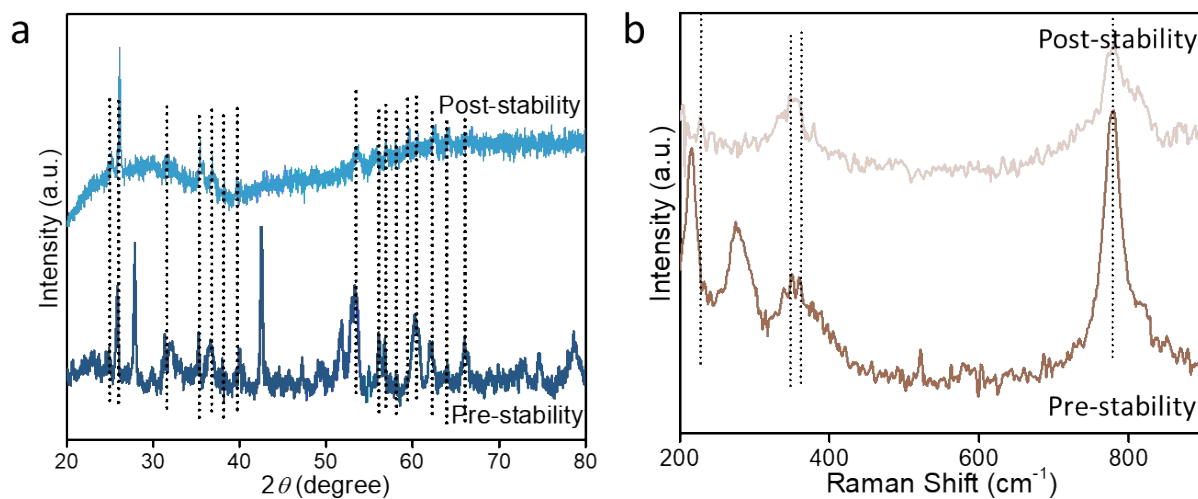
Figure S19. Post-stability (a) XRD and (b) Raman specta of MO@FO.
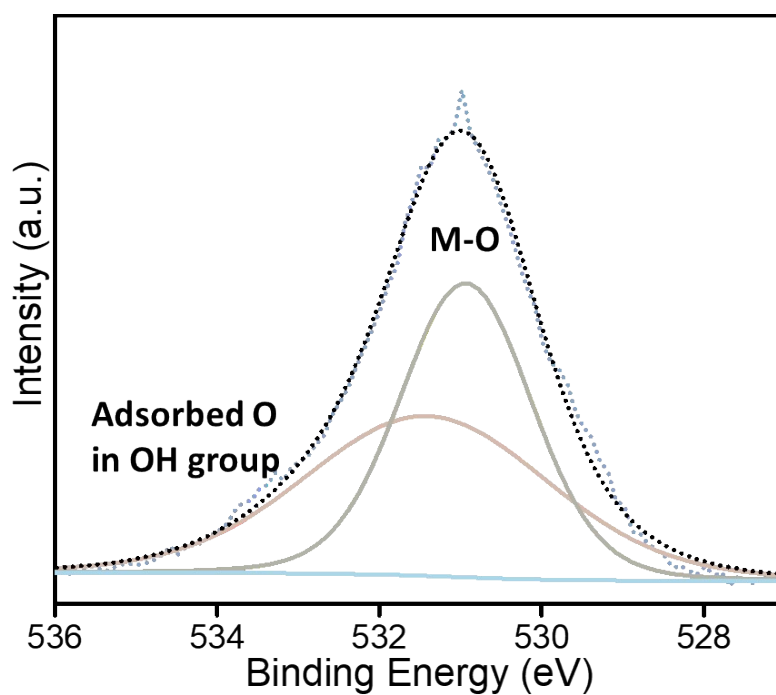
Figure S20. O 1s XPS spectrum for MO@FO after testing in 1M SW with 0.05 mM Iron nitrate salt.
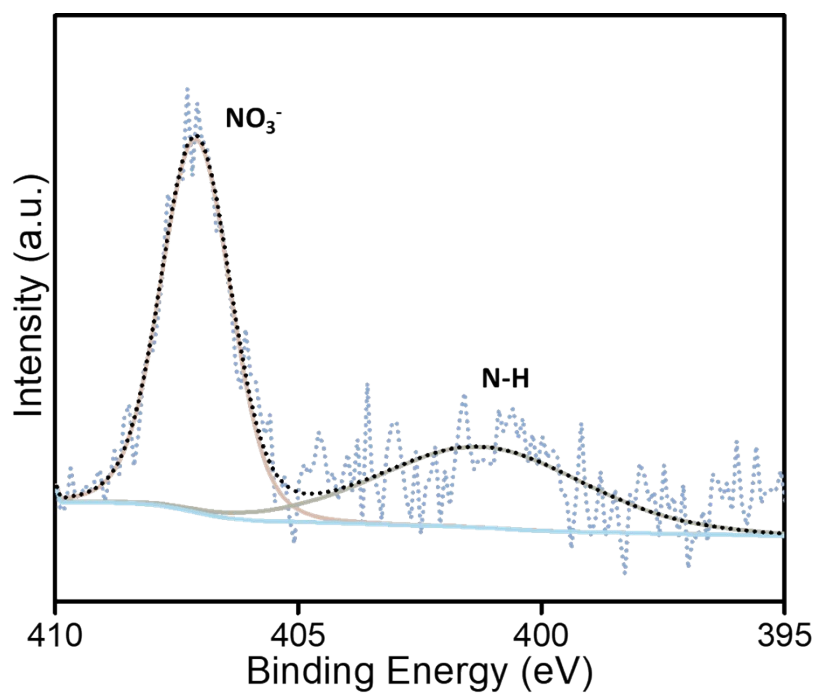
Figure S21. N 1s XPS spectrum for MO@FO after testing in 1M SW with 0.05 mM Iron nitrate salt.
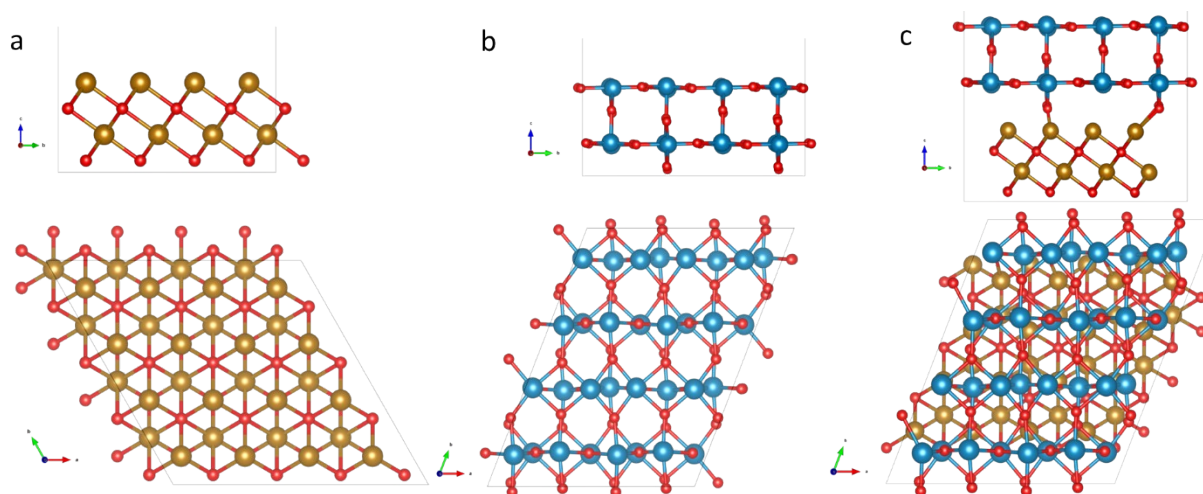
Figure S22. Side and top views of model (a) FeO(111) (b) MoO$_2$(-111) surfaces and (c) MoO$_2$@FeO heterostructure.
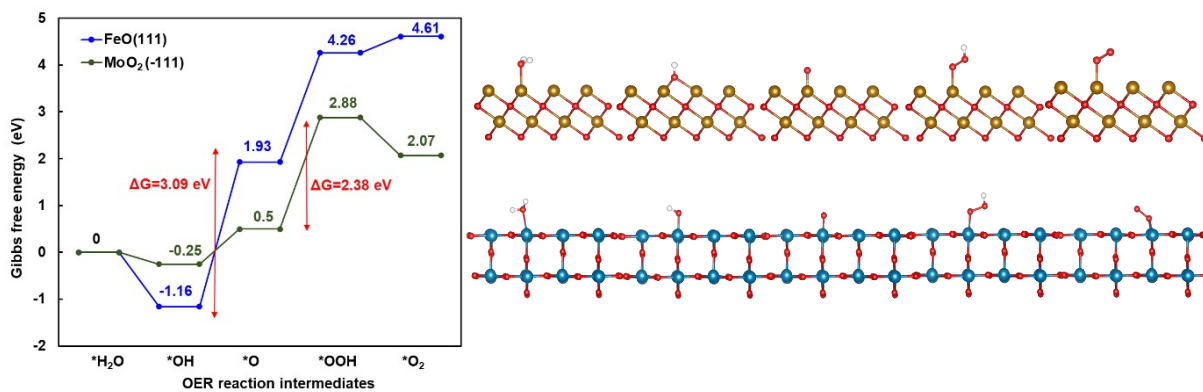
Figure S23: Free energy diagram of OER in alkaline condition on FeO(111) and MoO_2(-111) represented in blue and green lines respectively, with corresponding optimized geometries of OER intermediates of FeO (top) and MoO_2 (bottom).

MO@FO-Cl (E_{ad} = -2.69 eV)

MO@FO$_{NO_3}$-Cl (E_{ad} = -1.75 eV)
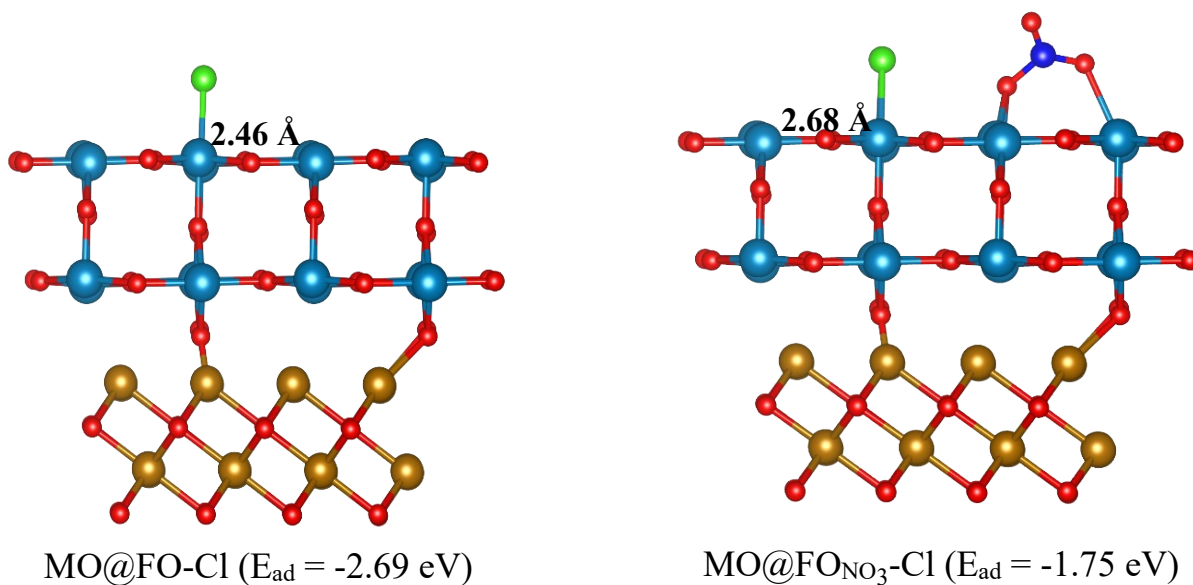
Figure S24: MO@FO heterostructure showing *Cl adsorption in the absence and presence of NO_3^- anion, the Mo-Cl bond represented in the figure.

Table S1. Overpotential comparison of MO@FO with the other catalysts reported in the literature in seawater/simulated seawater.

Sample	Catalyst	Overpotential (mV @mA cm^{-2})	Electrolyte	Reference
1	**MO@FO**	**290 mV @100 mA cm^{-2}**	**1 M KOH in seawater**	**This Work**
2	PW–OA–RuO$_x$@C	158 mV @10 mA cm^{-2}	0.5 M H$_2$SO$_4$ in seawater	[1]
3	Ti@TiN/Ni–Fe-LDH	250 mV @100 mA cm^{-2}	Simulated seawater (1 M KOH + 0.5 M NaCl)	[2]
4	15%-WO$_3$·xH$_2$O-in-MIL-88	360 mV @ 10 mA cm^{-2}	Alkaline seawater	[3]
5	N-NiMo$_3$P	346 mV @10 mA cm^{-2}	1 M KOH in seawater	[4]
6	Co–CoO@C	374 mV @10 mA cm^{-2}	1 M KOH in seawater	[5]
7	Pd-doped CoNPs@C	429 mV @100 mA cm^{-2}	Simulated seawater (1 M KOH + 0.6 M NaCl)	[6]
8	Ni$_x$Cr$_y$O	370 mV @100 mA cm^{-2}	1 M KOH in seawater	[7]
9	Co$_{3-x}$Pd$_x$O$_4$	370 mV @10 mA cm^{-2}	pH-neutral simulated seawater	[8]
10	60Fe/NF	254 mV @10 mA cm^{-2}	1 M KOH in seawater	[9]
11	RuO$_2$/NiFeOOH	273.5 mV @100 mA cm^{-2}	1 M KOH in seawater	[10]

Table S2. EIS data fitting parameters

Sample	R1	R2	CPE1
MO@FO	0.25	2.025	0.975
Fe$_2$O$_3$	2.23	1.648	0.814
MoO$_2$	1.741	2.128	0.781

Table S3. ICP-MS results showing Mo and Fe content in seawater electrolytes before and after stability testing.

Sample	Mo (ppb)	Fe (ppb)
ICP-MS Standard solution	0.041	0.466
1 M KOH in seawater	0.078	0.466
1 M KOH in seawater after stability testing	42.876	209.46
1 M KOH in seawater + iron nitrate salt before stability testing	0.066	165.427
1 M KOH in seawater + iron nitrate salt after 1000 h stability testing	5.097	175.067 (only 9.64 ppb difference)

Table S4. Sample parameters obtained from the polarization curves in 5% NaCl in DI water.

Sample	E_{corr} (V)	I_{corr} ($\mu A\ cm^{-2}$)	corrosion rate ($\mu m/year$)
MO@FO	-0.759	0.009	0.036
Fe_2O_3	-0.778	0.012	0.048
MoO_2	-0.779	0.014	0.056

$$Corrosion\ rate = \frac{I_{corr}}{area}$$

Where area = area of the working electrode

Table S5: Calculated water adsorption energy and closest metal-oxygen bond lengths on the oxide surfaces and MO@FO heterostructure.

Surface	M-O Distance (Å)	Adsorption energy (eV)	OER limiting potentials (V)
FeO(111)	2.14	-0.86	-1.90
MoO2(-111)	2.31	-1.06	-3.90
MO@FO	2.29	-1.16	-2.37

References

[1]   J. Ding, Z. Peng, Z. Wang, C. Zeng, Y. Feng, M. Yang, G. Hu, J. Luo, X. Liu, *J. Mater. Chem. A* **2024**, *12*, 28023-28031.

[2]   W. Yoon, Y. H. Park, X. Jin, S.-J. Hwang, *J. Mater. Chem. A* **2024**, *12*, 21016-21024.

[3]   Z. Huang, W. Shao, Y. Zheng, J. Wang, M. Wang, S. Li, X. Xu, C. Cheng, C. Zhao, *J. Mater. Chem. A* **2024**, *12*, 19968-19978.

[4]   S. Loomba, M. W. Khan, M. Haris, S. M. Mousavi, A. Zavabeti, K. Xu, A. Tadich, L. Thomsen, C. F. McConville, Y. Li, S. Walia, N. Mahmood, *Small* **2023**, *19*, 2207310.

[5]   S. Fathima T.K, A. Ghosh, S. Ramaprabhu, *Int. J. Hydrogen Energy* **2024**, *49*, 780-793.

[6]   Z. K. Ghouri, D. J. Hughes, K. Ahmed, K. Elsaid, M. M. Nasef, A. Badreldin, A. Abdel-Wahab, *Sci. Rep.* **2023**, *13*, 20866.

[7]   A. Malek, Y. Xue, X. Lu, *Angew. Chem.* **2023**, *135*, e202309854.

[8]   N. Wang, P. Ou, S. F. Hung, J. E. Huang, A. Ozden, J. Abed, I. Grigioni, C. Chen, R. K. Miao, Y. Yan, *Adv. Mater.* **2023**, *35*, 2210057.

[9]   Y. Zhuo, D. Liu, L. Qiao, S. Chen, J. Lu, W. F. Ip, H. Pan, Z. Wang, *Adv. Energy Mater.* **2023**, *13*, 2301921.

[10]   G. Chang, Y. Zhou, J. Wang, H. Zhang, P. Yan, H. B. Wu, X. Y. Yu, *Small* **2023**, *19*, 2206768.

[11]   G. Kresse, J. Furthmüller, *Comput. Mater. Sci.*, **1996**, 6, 15-50.

[12]   G. Kresse, J. Furthmüller, *Phys. Rev. B.,* **1996**, 54, 11169-11186.

[13]   J.P. Perdew, K. Burke, M. Ernzerhof, *Phys. Rev. Lett.*, **1996**, 77, 3865-3868.

[14]   S. Grimme, S. Ehrlich, L. Goerigk, *J. Comput. Chem.,* **2011**, 32, 1456.